Micro-/macro-responses of a ferroelectric single crystal with domain pinning and depinning by dislocations

H. H. Wu, J. Wang, S. G. Cao, L. Q. Chen, and T. Y. Zhang

Citation: Journal of Applied Physics **114**, 164108 (2013); doi: 10.1063/1.4826532
View online: http://dx.doi.org/10.1063/1.4826532
View Table of Contents: http://scitation.aip.org/content/aip/journal/jap/114/16?ver=pdfcov
Published by the AIP Publishing

Micro-/macro-responses of a ferroelectric single crystal with domain pinning and depinning by dislocations

H. H. Wu,[1] J. Wang,[2] S. G. Cao,[1] L. Q. Chen,[3] and T. Y. Zhang[1,a)]
[1]*Department of Mechanical and Aerospace Engineering, The Hong Kong University of Science and Technology, Clear Water Bay, Kowloon, Hong Kong*
[2]*Department of Engineering Mechanics, School of Aeronautics and Astronautics, Zhejiang University, Hangzhou 310027, China*
[3]*Department of Materials Science and Engineering, The Pennsylvania State University, University Park, Pennsylvania 16802, USA*

(Received 11 August 2013; accepted 6 October 2013; published online 30 October 2013)

Phase field simulations are conducted to investigate the micro-structural signature and the macro-response of a ferroelectric single crystal with domain pinning and depinning phenomena by dislocation arrays. It is shown that due to the presence of the dislocation arrays, a domain with polarizations antiparallel to an applied field can survive under the small amplitude of applied field. The residual domain serves as a pre-existing nucleus during the following macroscopic switching via only domain wall motion. The pinned domain will be depinned when the external electric field amplitude exceeds a critical value, which highly depends on the dislocation spacing in the dislocation array. Due to the pinning and depinning effect, an asymmetric hysteresis loop of polarization versus electric field might appear when a bias field is applied. © *2013 AIP Publishing LLC*. [http://dx.doi.org/10.1063/1.4826532]

I. INTRODUCTION

Ferroelectric materials have attracted much attention due to their distinguished electromechanical coupling properties and wide application in industry.[1,2] An important characteristics of ferroelectric materials is the hysteresis loop of polarization versus applied electric field, which stems from the switching of spontaneous polarization. The polarization switching is directly related to the performance of ferroelectric nonvolatile memories. The hysteresis loops are characterized by the remanent polarization and the coercive field, which are highly dependent on the domain structure, the nucleation of domains with reversed polarization, and domain wall mobility. Defects such as space charges,[3,4] dislocations,[5–9] grain boundaries,[10,11] and crack tips[12,13] are potential nucleation sites of new domains during polarization switching. An in-depth understanding of the role of different defects in polarization switching is urgently necessary to improve the ferroelectric properties and to prevent the degradation of ferroelectric devices, including fatigue fracture, imprint, and aging effect.[14–18]

Dislocations are one of the most common defects, which can be introduced into ferroelectric bulk and thin films[5–8] during the fabrication at high temperature. The pre-existed dislocations play important roles in the ferroelectric switching, acting as nucleation sites of new domains or/and pinning the domain wall motion. For example, the *in situ* transmission electron microscopy (TEM) observations show that a pinning force is exerted on the domain wall by dislocations during the nucleation and growth of new domains in a tetragonal $PbZr_{0.2}Ti_{0.8}O_3$ thin film subjected to an applied electric field.[9] Due to the effect of dislocation wall, the ferroelectric properties can be greatly improved by reducing the coercive field and meanwhile enhancing the remanent polarization if an appropriate density of dislocations is introduced at high temperature.[25]

Although it is known that dislocations alter the ferroelectric properties, it is quite difficult in experiments to identify the role played by dislocations in the domain switching, especially in the new domain nucleation and domain wall pinning. Few theoretical works have investigated the role of dislocations. By using the phase field model, the effect of interfacial dislocations on the paraelectric (PE) loop and the domain structure of ferroelectric thin film was investigated.[19–22] With pre-existed bi-domain structures of 180°/90° domain walls, Kontsos and Landis[22] investigated the interactions between domain walls and an array of dislocations and the pinning strength of the dislocations on domain wall in ferroelectric single crystals by using finite element based phase field approach.

In phase field simulations of a finite ferroelectric representative cell with periodic boundary conditions, the stress field induced by polarizations is calculated usually in Fourier space, because the calculation is fast and convenient. However, if the stress field of a dislocation in a finite representative cell with periodic boundary conditions was solved in Fourier space with Mura's dislocation eigenstrain approach, the stress field exhibited a significant oscillation.[23] This is because Mura's dislocation eigenstrain method[24] is valid for an infinite domain, rather than for a finite representative cell. To get rid of the oscillation, the Burgers vector was replaced by a Gaussian function of Burgers vector distribution. Since analytic solution of the stress field in real space is available for a 2D periodic dislocation array,[25] in the present work, we shall use the analytic solution in real space for

a)Author to whom correspondence should be addressed. Electronic mail: mezhangt@ust.hk. Tel.: +852 2358 7192. Fax: +852 2358-1543.

dislocation stress field and solve the stress field of polarizations in Fourier space. This hybrid approach takes both advantages of the analytic solution and the Fourier transformation, thereby enhancing the simulation efficiency.

In a previous work,[25] phase field simulations are performed to investigate the effect of dislocation arrays on the nonlinear electromechanical properties of ferroelectric single crystal. Following the previous work, this paper aims at a better understanding on the complex role of dislocations in domain pinning and depinning in ferroelectrics subjected to different amplitude of external electric fields. More attention will be paid to the relationship between micro-structural signature and the macro-response due to domain pinning and depinning.

II. NUMERICAL METHODOLOGY

A. General approach

The paraelectric to ferroelectric phase transition occurs in a ferroelectric material when temperature is lower than the Curie point. The polarization, $\mathbf{P} = (P_1, P_2, P_3)$, is usually used as the order parameter in phase field simulations of ferroelectrics, although other variants can also be used as the order parameter.[26] The domain configuration and polarization switching are a direct consequence of the minimization process of the total free energy of a whole simulated system, which is a function of the polarization, polarization gradient, strain, and electric field. The temporal evolution of polarization is described by the time dependent Ginzburg-Landau (TDGL) equation

$$\frac{\partial P_i(\boldsymbol{x},\mathrm{t})}{\partial t} = -L\frac{\delta F}{\delta P_i(\boldsymbol{x},\mathrm{t})}, \quad (i = 1, 2, 3), \tag{1}$$

where L is the kinetic coefficient, F is the total energy of the system, $\delta F/\delta P_i(\boldsymbol{x},t)$ is the thermodynamic driving force for the spatial and temporal evolution of $P_i(\boldsymbol{x},t)$, and $\boldsymbol{x} = (x_1, x_2, x_3)$ denotes the spatial vector. The total free energy can be expressed as

$$F = \int_V [f_{Land}(P_i) + f_{elas}(P_i, \varepsilon_{ij}) + f_{grad}(P_{i,j}) + f_{elec}(P_i, E_i^{ex})]dV. \tag{2}$$

In Eq. (2), the Landau free energy density f_{Land} is given by

$$\begin{aligned} f_{Land}(P_i) = {} & \alpha_1(P_1^2 + P_2^2 + P_3^2) + \alpha_{11}(P_1^4 + P_2^4 + P_3^4) \\ & + \alpha_{12}(P_1^2P_2^2 + P_2^2P_3^2 + P_1^2P_3^2) \\ & + \alpha_{111}(P_1^6 + P_2^6 + P_3^6) + \alpha_{112}[P_1^4(P_2^2 + P_3^2) \\ & + P_2^4(P_1^2 + P_3^2) + P_3^4(P_1^2 + P_2^2)] + \alpha_{123}P_1^2P_2^2P_3^2, \end{aligned} \tag{3}$$

where $\alpha_1 = (T - T_0)/2\kappa_0 C_0$, α_{12}, α_{111}, α_{112}, and α_{123} are constant coefficients, T and T_0 denote the temperature and Curie-Weiss temperature, respectively, C_0 is the Curie constant, and κ_0 is the dielectric constant of vacuum. The elastic energy density takes the form of

$$f_{elas} = \frac{1}{2}c_{ijkl}\varepsilon_{ij}^{elas}\varepsilon_{kl}^{elas}, \tag{4}$$

where c_{ijkl} are the elastic constants and ε_{ij}^{elas} are the elastic strains, which includes two parts. The first part of the elastic strains are induced by polarizations and is given by $\varepsilon_{ij}^{p,elas} = (\varepsilon_{ij}^{p} - \varepsilon_{ij}^{0})$, where ε_{ij}^{p} are the total strains produced by polarizations only and ε_{ij}^{0} are the spontaneous strains or the eigenstrains of polarizations. The spontaneous strains have the form as $\varepsilon_{ij}^{0} = Q_{ijkl}P_kP_l$, where Q_{ijkl} are the electrostrictive coefficients. The spontaneous strains are similar to the thermal expansion strains in thermal stress analysis. The other part of the elastic strains, ε_{ij}^{d}, is produced by dislocations. Thus, the elastic strains are given by

$$\varepsilon_{ij}^{elas} = \varepsilon_{ij}^{p} - \varepsilon_{ij}^{0} + \varepsilon_{ij}^{d}. \tag{5}$$

With the periodic boundary condition, the general solution of the total displacement field induced by polarizations is given in Fourier space by[27,28]

$$u_i^p(\boldsymbol{\xi}) = X_jN_{ij}(\boldsymbol{\xi})/D(\boldsymbol{\xi}), \tag{6}$$

where $X_i = -ic_{ijkl}\varepsilon_{kl}^{0}\xi_j$, $i = \sqrt{-1}$, $N_{ij}(\boldsymbol{\xi})$ are cofactors of a 3×3 matrix $\boldsymbol{K}(\boldsymbol{\xi})$

$$\boldsymbol{K}(\boldsymbol{\xi}) = \begin{bmatrix} K_{11} & K_{12} & K_{13} \\ K_{21} & K_{22} & K_{23} \\ K_{31} & K_{32} & K_{33} \end{bmatrix}, \tag{7}$$

and $D(\boldsymbol{\xi})$ is the determinant of matrix $\boldsymbol{K}(\boldsymbol{\xi})$. Note that $K_{ki}(\boldsymbol{\xi}) = c_{kjil}\xi_j\xi_l$, in which ξ_i are the coordinates in Fourier space. The corresponding strains are obtained from

$$\varepsilon_{ij}^{p} = \frac{1}{2}\left\{\frac{\partial u_i^p}{\partial x_j} + \frac{\partial u_j^p}{\partial x_i}\right\}. \tag{8}$$

The dislocation-induced displacement $\mathbf{u}^{\mathrm{d}}$ is obtained from the Stroh formalism[33] for the pure dislocation problem without any polarizations, which is given in Sec. II B. The elastic strain induced by dislocations, ε_{ij}^{d}, is obtained from

$$\varepsilon_{ij}^{d} = \frac{1}{2}\left\{\frac{\partial u_i^d}{\partial x_j} + \frac{\partial u_j^d}{\partial x_i}\right\}. \tag{9}$$

Both the polarization-induced strains, ε_{ij}^{p}, and the elastic strain induced by dislocations, ε_{ij}^{d}, are calculated from the corresponding displacements. Because the strains and stresses produced by polarizations and dislocations are both calculated based on linear elasticity, the superposition principle is valid, and the polarization-induced elastic strains and dislocation-induced strains are compatible.

The gradient energy density can be expressed as

$$f_{grad} = \frac{1}{2}g_{ijkl}\frac{\partial P_i}{\partial x_j}\frac{\partial P_k}{\partial x_l}, \tag{10}$$

where g_{ijkl} are the gradient energy coefficients. The gradient energy gives the energy penalty for spatially inhomogeneous polarization. The electrical energy density includes the self-electrostatic energy density and the energy induced by the external electric field, which can be expressed as

$$f_{elec} = -\frac{1}{2}E_i P_i - E_i^{ex} P_i, \tag{11}$$

where E_i and E_i^{ex} are the self-electrostatic electric field and external applied electric field, respectively. The self-electrostatic field is the negative gradient of the electrostatic potential ϕ, i.e., $E_i = -\partial\phi/\partial x_i$. The electrostatic potential is obtained by solving the following electrostatic equilibrium:

$$\kappa_0\left(\frac{\kappa_{11}\partial^2\phi}{\partial x_1^2} + \frac{\kappa_{22}\partial^2\phi}{\partial x_2^2} + \frac{\kappa_{33}\partial^2\phi}{\partial x_3^2}\right) = \frac{\partial P_1}{\partial x_1} + \frac{\partial P_2}{\partial x_2} + \frac{\partial P_3}{\partial x_3}, \tag{12}$$

where κ_{ij} are the background dielectric constants of the material.[29–32] With the periodic boundary condition, Eq. (12) is analytically solved in Fourier space, which is similar to the method used in solving the mechanical equilibrium equation.

B. The stress/strain field of dislocation arrays

In two-dimensional anisotropic linear elasticity, Stroh's formalism[33] gives the general solution

$$\mathbf{u}^d = \mathbf{A}\mathbf{f}(z_\alpha) + \overline{\mathbf{A}\mathbf{f}(z_\alpha)}, \tag{13a}$$

$$\psi = \mathbf{B}\mathbf{f}(z_\alpha) + \overline{\mathbf{B}\mathbf{f}(z_\alpha)}, \tag{13b}$$

where $\mathbf{u}^d$ and ψ are the displacement and stress function vectors, respectively, $\mathbf{A}$ and $\mathbf{B}$ are the eigenvector matrices determined by the elastic constants and orientation of the ferroelectric crystal, $\mathbf{f}(z_\alpha) = [f_1(z_1)f_2(z_2)f_3(z_3)]^T$ is an analytic vector of $z_\alpha = x_1 + p_\alpha x_2$ ($\alpha = 1, 2, 3$), and p_α with $\mathrm{Im}(p_\alpha)$ is the eigenvalue of the eigen-equation

$$\mathbf{N}\eta = p_\alpha \eta. \tag{14a}$$

In Eq. (14a),

$$\eta = \begin{pmatrix} A \\ B \end{pmatrix} \tag{14b}$$

is the eigenvector with A and B being the column vectors of $\mathbf{A}$ and $\mathbf{B}$, respectively, and the matrix $\mathbf{N}$ is given by

$$\mathbf{N} = \begin{pmatrix} \mathbf{N}_1 & \mathbf{N}_2 \\ \mathbf{N}_3 & \mathbf{N}_1^T \end{pmatrix}, \tag{14c}$$

with

$$\mathbf{N}_1 = -\mathbf{T}^{-1}\mathbf{R}^T, \quad \mathbf{N}_2 = \mathbf{T}^{-1} = \mathbf{N}_2^T, \quad \mathbf{N}_3 = \mathbf{R}\mathbf{T}^{-1}\mathbf{R}^T - \mathbf{Q} = \mathbf{N}_3^T, \tag{14d}$$

where

$$Q_{ik} = c_{i1k1}, R_{ik} = c_{i1k2}, T_{ik} = c_{i2k2}. \tag{14e}$$

Matrices $\mathbf{A}$ and $\mathbf{B}$ have the following properties:

$$\mathbf{A}\mathbf{A}^T + \overline{\mathbf{A}\mathbf{A}^T} = \mathbf{B}\mathbf{B}^T + \overline{\mathbf{B}\mathbf{B}^T} = 0, \tag{15a}$$

$$\mathbf{B}\mathbf{A}^T + \overline{\mathbf{B}\mathbf{A}^T} = \mathbf{A}\mathbf{B}^T + \overline{\mathbf{A}\mathbf{B}^T} = \mathbf{I}, \tag{15b}$$

where $\mathbf{I}$ is the identity matrix. The stress field is calculated from the stress function vector ψ as

$$\sigma_{i2} = \psi_{i,1}, \quad \sigma_{i1} = -\psi_{i,2}. \tag{16}$$

For a straight line dislocation located at z_α^d in an infinite body, the two dimensional solution is given with the analytic vector in the form of

$$\mathbf{f}(z_\alpha) = \ln(z_\alpha - z_\alpha^d)\frac{1}{2\pi i}\mathbf{B}^T\mathbf{b}, \tag{17}$$

where the angle bracket denotes a diagonal matrix and $\mathbf{b} = (b_1, b_2, b_3)^T$ is the burgers vector of the dislocation.

If there is only a dislocation of Burgers vector $\mathbf{b}_i$ located at $x_{1,i}$ and $x_{2,i}$ in the representative cell, we use superposition and have the analytic vector[33]

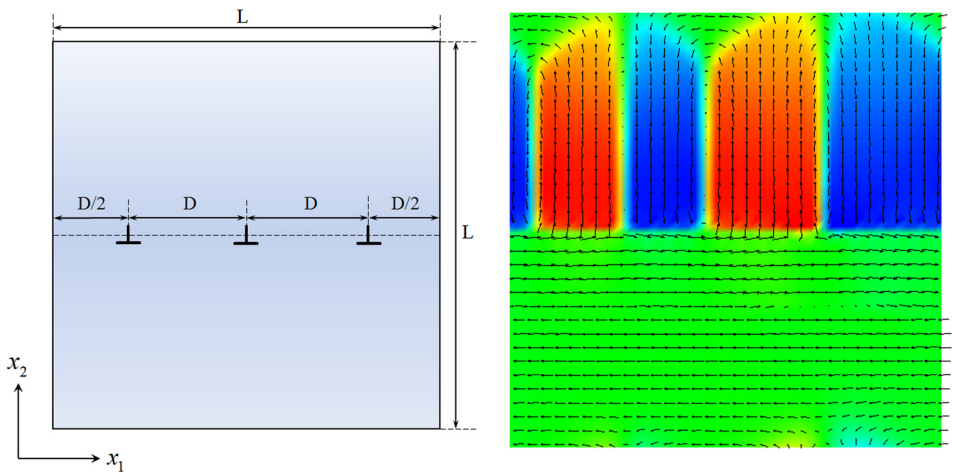

FIG. 1. Schematic diagram of the simulated cell with a dislocation wall (left) and the initial stable domain structure with DLD = 21 (right).

$$\mathbf{f_i} = \left\langle \sum_{m=-\infty}^{\infty} \sum_{n=-\infty}^{\infty} \ln\{(x_1 + p_\alpha x_2) - [(mL_{x1} + p_\alpha nL_{x_2}) + (x_{1,i} + p_\alpha x_{2,i})]\} \right\rangle \times \frac{1}{2\pi i} \boldsymbol{B}^T \mathbf{b}_i, \tag{18}$$

where L_{x_1} and L_{x_2} are the dimensions of the representative cell in the x_1 and x_2 directions, respectively. The analytical vector $\mathbf{f}$ for n dislocations in the representative cell is thus given by

$$\mathbf{f} = \sum_{i=1}^{n} \mathbf{f}_i. \tag{19}$$

Substituting Eq. (19) into Eq. (13a) yields the displacements generated by the dislocations. Then, using the strain-displacement equation of Eq. (9), we have the dislocation induced strain field.

C. Simulation model

For convenience, the following normalized variables and coefficients are employed in the present study:[27]

$$\boldsymbol{x}^* = \sqrt{|\alpha_1|/G_{110}}\boldsymbol{x}, t^* = |\alpha_1|Lt, \mathbf{P}^* = \mathbf{P}/P_0, \kappa_0^* = \kappa_0|\alpha_1|, \alpha_1^* = \alpha_1/|\alpha_1|, \alpha_{11}^* = \alpha_{11}P_0^2/|\alpha_1|,$$
$$\alpha_{12}^* = \alpha_{12}P_0^2/|\alpha_1|, \alpha_{111}^* = \alpha_{111}P_0^4/|\alpha_1|, \alpha_{112}^* = \alpha_{112}P_0^4/|\alpha_1|, \alpha_{123}^* = \alpha_{123}P_0^4/|\alpha_1|, Q_{11}^* = Q_{11}P_0^2,$$
$$Q_{12}^* = Q_{12}P_0^2, Q_{44}^* = Q_{44}P_0^2, c_{11}^* = c_{11}/(|\alpha_1|P_0^2), c_{12}^* = c_{12}/(|\alpha_1|P_0^2), c_{44}^* = c_{44}/(|\alpha_1|P_0^2),$$
$$G_{11}^* = G_{11}/G_{110}, G_{12}^* = G_{12}/G_{110}, G_{44}^* = G_{44}/G_{110}, G_{44}^{'*} = G_{44}^{'}/G_{110}, E^{\mathrm{ex},*} = E^{\mathrm{ex}}/(|\alpha_1|P_0),$$

where $P_0 = |P_0| = 0.757\mathrm{C/m}^2$ is the magnitude of the spontaneous polarization at room temperature, $\alpha_1 = \frac{T-T_0}{2\varepsilon_0 C_0} = (25 - 479) \times 3.8 \times 10^5\,\mathrm{m}^2\,\mathrm{N/C}^2$ and $G_{110} = 1.73 \times 10^{-10}\,\mathrm{m}^4\,\mathrm{N/C}^2$ is a reference value of the gradient energy coefficients. The Voigt notations are used for the elastic stiffness tensors. The values of the normalized material coefficients of $PbTiO_3$ used in the simulations can be found in the previous papers.[27,28]

With the dimensionless variables and Eq. (2), the time-dependent Ginzburg-Landau equation (1) can be expressed as

$$\frac{\partial P_i^*(\boldsymbol{x}^*, t^*)}{\partial t^*} = -\frac{\delta \int [f_{land}(P_i^*) + f_{elas}(P_i^*, \varepsilon_{kl}^*) + f_{elec}(P_i^*, E_i^*, E_i^{ex,*})]dV^*}{\delta P_i^*} - \frac{\delta \int f_{grad}(P_{i,j}^*)dV^*}{\delta P_i^*}. \tag{20}$$

In Fourier space, Eq. (20) takes the form

$$\frac{\partial}{\partial t^*}\hat{P}_i(\boldsymbol{\xi}, t^*) = -\{\hat{f}(P_i^*)\}_\xi - G_i\hat{P}_i(\boldsymbol{\xi}, t^*), \tag{21}$$

where $\hat{P}_i(\boldsymbol{\xi}, t^*)$ and $\{\hat{f}(P_i^*)\}_\xi$ are the Fourier transformations of $P_i^*(\boldsymbol{x}^*, t^*)$ and $\frac{\delta \int [f_{Land}(P_i^*) + f_{elas}(P_i^*, \varepsilon_{kl}^*) + f_{elec}(P_i^*, E_i^{ex*})]dV^*}{\delta P_i^*}$, respectively, G_i are the gradient operators correspond to the ith-component of the polarization field, which are defined as follows:

$$\begin{aligned} G_1 &= G_{11}^*\xi_1^2 + (G_{44}^* + G_{44}^{'*})(\xi_2^2 + \xi_3^2), \\ G_2 &= G_{11}^*\xi_2^2 + (G_{44}^* + G_{44}^{'*})(\xi_1^2 + \xi_3^2), \\ G_3 &= G_{11}^*\xi_3^2 + (G_{44}^* + G_{44}^{'*})(\xi_2^2 + \xi_1^2). \end{aligned} \tag{22}$$

The semi-implicit Fourier-spectral method is employed to solve the partial differential equation (21) in the present work.[34]

In the present study, two dimensional (2D) phase field simulation were conducted under plane strain condition. Fig. 1 (Left) is a schematic drawing of the simulated cell with 64 × 64 discrete grids. The normalized size of grid is $\Delta x_1^* = \Delta x_2^* = 0.8$, where the x_1 and x_2 axes are set along the pseudo cubic crystallographic [100] and [010] directions, respectively. A dislocation array composed of periodically distributed dislocations with the same Burgers vector of $\frac{\Delta x_1^*}{2}$[100] is allocated at the middle of the simulated cell. The dislocation spacing and the simulated cell dimension are denoted by D and L, respectively, giving the Dislocation Linear Density (DLD) of L/D. For the maximum DLD studied, the dislocation spacing is 2.4 nm, which is close to the experimentally observed value of 2.7 nm.[6] The periodic boundary condition is adopted in both x_1 and x_2 directions, implying that the simulated cell is within an infinitely large 2D single crystal with periodically distributed dislocation arrays. The normalized formula and the material constants of $PbTiO_3$ single crystal at room temperature are given in the previous paper.[25] A random distribution of initial polarizations with the maximum magnitude less than 0.0005 is assigned to the simulated system to trig the polarization evolution, which leads to the initial domain structure after 20 000-steps-evolution with a time step of $\Delta t^* = 0.04$ as shown in the right plot of Fig. 1.

As mentioned above, the simulations were conducted at fixed dimensions. Thus, macroscopically average strains should remain zero or pre-described values during the evolution calculations. However, fixed dimensions cause macroscopically average stresses to change during domain structure evolution. To present the simulation results in a conventional manner, we convert macroscopically average stresses to macroscopically average strains via Hook's law. Without any applied mechanical loads, from Eq. (5) and Hook's law, we have the stresses

$$\sigma_{kl}^{(s)} = c_{ijkl}\varepsilon_{ij}^{ela} = c_{ijkl}(\varepsilon_{ij}^{p} - \varepsilon_{ij}^{0} + \varepsilon_{ij}^{d}). \tag{23}$$

Since we fixed the dimensions in the simulations, the average strains, $\langle\varepsilon_{ij}^{p}\rangle$, were all zero. The average strains, $\langle\varepsilon_{ij}^{0} - \varepsilon_{ij}^{d}\rangle$, were then determined from the average stresses, $\langle\sigma_{ij}^{(s)}\rangle$

$$\langle\varepsilon_{ij}^{0} - \varepsilon_{ij}^{d}\rangle = -S_{ijkl}\langle\sigma_{kl}^{(s)}\rangle. \tag{24}$$

Eq. (24) indicates that the average strains, $\langle\varepsilon_{ij}^{0} - \varepsilon_{ij}^{d}\rangle$, represent the average stresses $\langle\sigma_{kl}^{(s)}\rangle$ induced by domain structure evolution under the condition of fixed dimensions. We may imagine that after the evolution, the average strains, $\langle\varepsilon_{ij}^{0} - \varepsilon_{ij}^{d}\rangle$, will be produced if we release the average stresses $\langle\sigma_{kl}^{(s)}\rangle$. In the present study, we use the average strain, $\langle\varepsilon_{22}^{0} - \varepsilon_{22}^{d}\rangle$, to represent the relative change in the dimension of a ferroelectric along the x_2 direction, i.e., along the applied field direction. The average strain, $\langle\varepsilon_{22}^{0} - \varepsilon_{22}^{d}\rangle$, could be obtained by using $\varepsilon_{ij}^{0} = Q_{ijkl}P_kP_l$ to calculate the value of $\langle\varepsilon_{22}^{0}\rangle$ at each point on the grid and then averaging $\langle\varepsilon_{22}^{0}\rangle$ over the simulated region, and $\langle\varepsilon_{22}^{d}\rangle$ is a constant during the polarization switching for the stationary nature of the dislocations at room temperature. Alternatively, the average strain, $\langle\varepsilon_{22}^{0} - \varepsilon_{22}^{d}\rangle$, could be obtained from the average stresses, $\langle\sigma_{kl}^{(s)}\rangle$, which were calculated by taking the average of the polarization-linked stresses, $\langle\sigma_{kl}^{(s)}\rangle$, at each point of the grid.

III. RESULTS AND DISCUSSION

A. The electromechanical response with different amplitudes of electric field

To investigate the polarization switching of the ferroelectric single crystal, the polarization response to external electric field is simulated at room temperature. A dimensionless external electric field $E_2^{ex,*} = \mathrm{E}_0^* \sin(4.5\pi i/180\,000)$ is applied along the x_2 direction, where i denotes the time step and E_0^* is the field amplitude. At each dimensionless time step of $\Delta t^* = 0.04$, the simulated system evolves once, and 180 000 time steps complete two and a quarter cycles of the switching. The average polarization along the electric field direction is taken as the macroscopic response of the simulated ferroelectric single crystal. The simulated hysteresis loops are quasistatic due to the large number of electric field varying steps in each cycle or the small change in electric field of each varying step.

Fig. 2(A) give the simulated hysteresis loops when the amplitude of dimensionless electric field is less than 0.7. The remanent polarization and coercive field are 0.085 and 0.097, respectively, quite small and correspondingly comparable to those of ferroelectric thin films constrained by the substrate.[35] When the amplitude of electric field decreases from 0.7 to 0.4, both remanent polarization and coercive field decrease to 0.039 and 0.058, respectively. On the other hand, when the amplitude of electric field exceeds a critical level of 0.8, the remanent polarization and coercive field increase abruptly to 0.45 and 0.23, respectively, as shown in

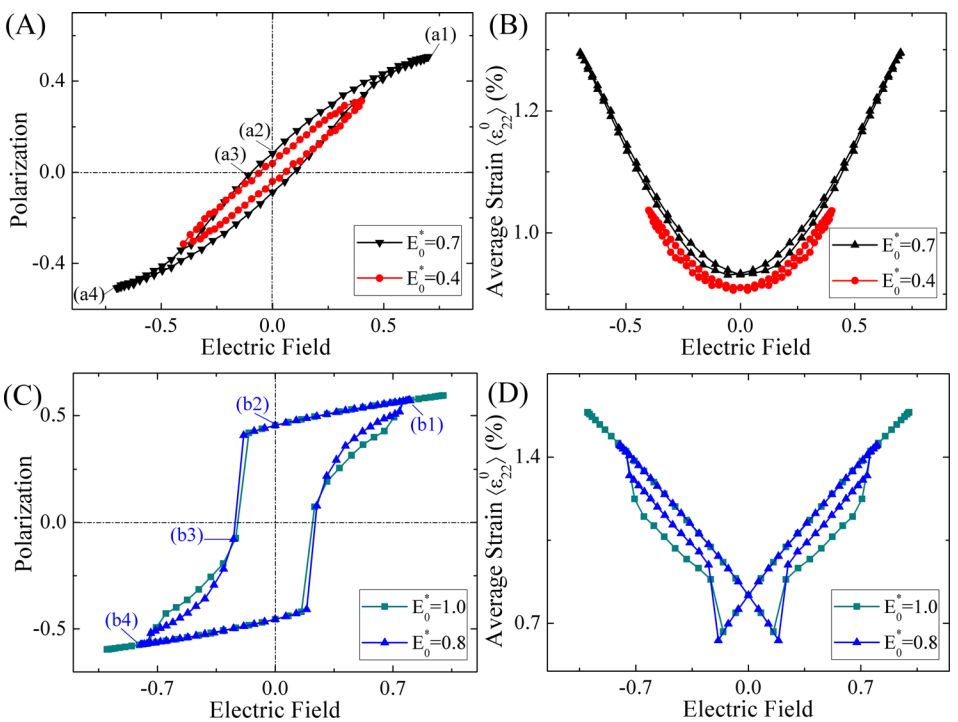

FIG. 2. PE loops (A) and (C) corresponding curves of average strain versus the electric field (B) and (D) for the ferroelectrics with the dislocation density of DLD = 21; where $\mathrm{E}_0^* = 0.4$ and 0.7 in (A) and (B) and $\mathrm{E}_0^* = 0.8$ and 1.0 in (C) and (D).

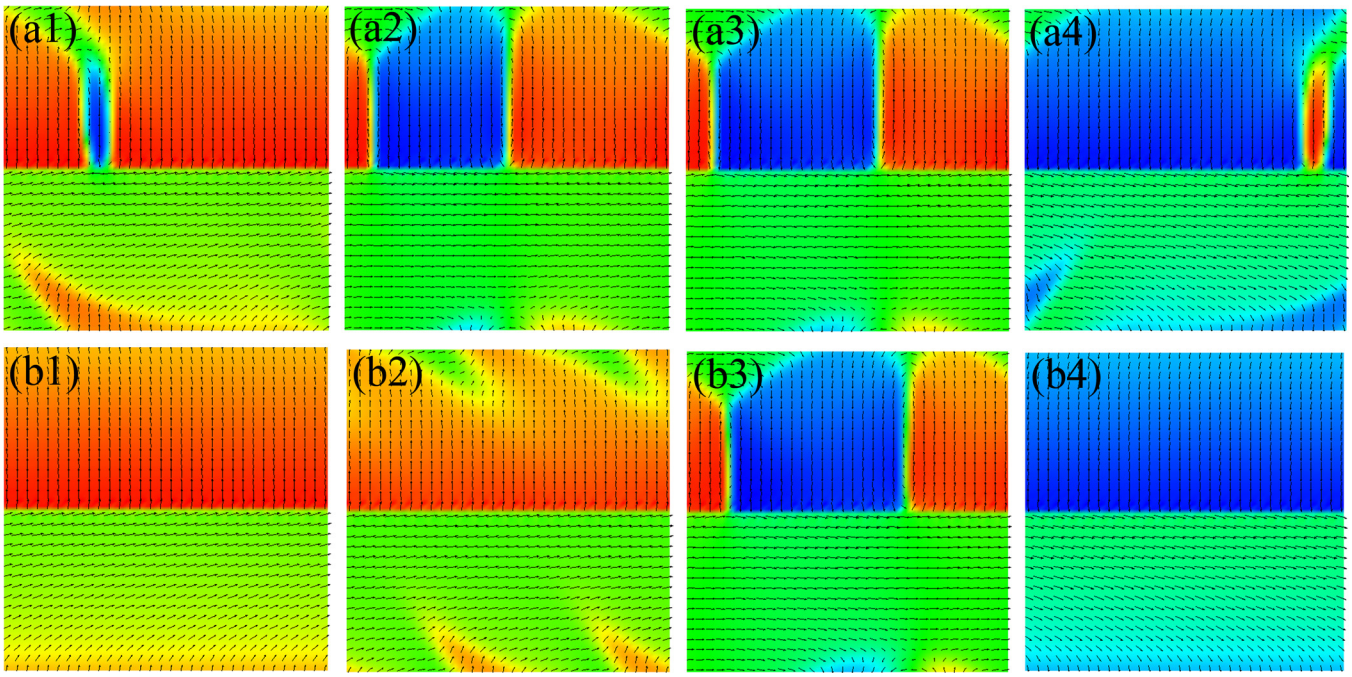

FIG. 3. Domain structures of (a1)–(a4) corresponding to points (a1)–(a4) on the curve of $E_0^* = 0.7$ in Fig. 2(A); domain structures of (b1)–(b4) corresponding to points (b1)–(b4) on the curve of $E_0^* = 0.8$ in Fig. 2(C). The domains antiparallel to external electric field in (a1) and (a4) are pinned by the dislocation array. In (b1) and (b4), the pinned domains are depinned due to the large electric field (enhanced online). [URL: http://dx.doi.org/10.1063/1.4826532.1] [URL: http://dx.doi.org/10.1063/1.4826532.2]

Fig. 2(C). When the amplitude of electric field increases from 0.8 to 1.0, the remanent polarization and coercive field change to 0.45 and 0.22, respectively. Obviously these changes are small again. Figs. 2(B) and 2(D) show the corresponding curves of average strain versus electric field, indicating also the significant difference between the strain versus electric field curves under $E_0^* = 0.7$ and $E_0^* = 0.8$.

Fig. 3 illustrates the polarization distributions at points (a1)–(a4) in the curve under $E_0^* = 0.7$ in Fig. 2(A) and points (b1)–(b4) in the curve under $E_0^* = 0.8$ in Fig. 2(C). The region below the dislocation array is almost a single domain with most polarizations along the horizontal direction, as shown in Figs. 3(a1)–(a4) and (b1)–(b4). This domain structure below the dislocation array makes a limited contribution to the macroscopic responses of the PE loops and the strain versus field curves. The limited contribution is through polarization rotation, as shown in Fig. 3. Above the dislocation array, most polarizations are along the vertical direction but form a multi-domain structure, which is responsible for the different hysteresis PE loops in Figs. 2(A) and 2(C). The strain mismatch between the vertical and horizontal domains at the dislocation array is accommodated by the strain induced by dislocations, which makes the below domain stable. Fig. 3(a1) shows that there is a domain antiparallel to the external electric field, indicating that the domain is pinned by the dislocation array. The domain pinning differs from the classical domain wall pinning, in which dislocations are allocated on a domain wall such that the domain wall cannot move. The domain pinning just means that a domain with polarizations antiparallel to an applied field can exist due to the presence of the dislocation array. Since the antiparallel domain exists, no domain nucleation is needed in the microscopic polarization switching. When the electric field decreases to zero, the antiparallel domain grows by domain wall motion, as shown in Fig. 3(a2). When the opposite electric field increases to the coercive field, the domain structure shown in Fig. 3(a3) remains almost the same as that in Fig. 3(a2). When the opposite electric field increases to the maximum value, most polarizations above the dislocation array are along the electric field direction, in which there is a domain with polarizations antiparallel to the electric field. Again, the domain is pinned by the dislocation array, which will serve as a seed domain for the next macroscopic switch. However, when the amplitude of electric field increases to $E_0^* = 0.8$, the driven force provided by the external electric field is large enough to completely align all polarizations above the dislocation array into a domain, as shown in Figs. 3(b1) and 3(b4). In this case, the antiparallel domain under $E_0^* = 0.7$ disappears totally under $E_0^* = 0.8$. We call this phenomenon the domain depinning by following the classical domain wall depinning. The present phase field simulations show that the dislocation array may pin some antiparallel domain if the applied field is low and the domain depinning occurs when the applied field is high. See movies 1 and 2 for the temporal evolution of the polarization switching processes for the cases of $E_0^* = 0.8$ and $E_0^* = 0.7$, in which the domain pinning and depinning process are clearly shown. It is the domain pining and depinning that causes the great change in the macroscopic PE and strain versus field curves.

Obviously, the domain pinning effect will be stronger if the DLD is higher. Fig. 4 shows the dependence of critical depinning electric field on the DLDs. When the DLD is lower than 10, the critical depinning electric field is almost the same as 0.2. This is because when the DLD is lower than 10, the collective action of dislocations in the array is negligible and each dislocation interacts with polarizations alone.

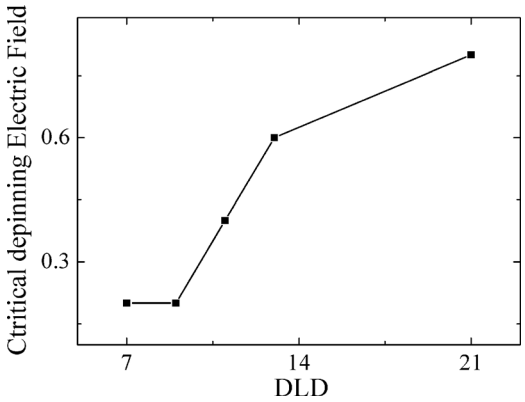

FIG. 4. The critical de-pinning electric field versus the DLD.

When the DLD exceeds 10, the dislocations exhibit the collective action and thus the critical depinning electric field increases with the DLD. In such a situation, due to the existence of the dislocation array, as long as the applied electric field is lower than the critical depinning electric field, the domain switching will be firmly lagged or pinned by the stress/ strain field of dislocations, as described above, and the lagged domain switching leads to both low remanent polarization and coercive field. However, once the applied electric field is higher than the critical electric field, the energy barrier brought by the dislocation array will be overcome and the polarization switching behavior will be greatly changed.

B. The electromechanical response with a bias field

In the present work, a bias field is applied by adding a constant field to the sinusoidal field and the applied electric field becomes

$$E^{ex,*} = \mathrm{E}_0^* \sin(4.5\pi i/180\,000) \pm 0.1,$$

where ± 0.1 denotes that the bias field is applied along the $\pm x_2$ axis with the dimensionless magnitude 0.1.

Fig. 5 shows the simulation results with DLD = 21. When the value of $\mathrm{E}_0^* + 0.1$ or $|-\mathrm{E}_0^* - 0.1|$ is smaller than the critical depinning electric field, the dislocations pin the antiparallel domain and the PE curves do not exhibit too much hysteresis, as shown in Fig. 5(A). When the value of $\mathrm{E}_0^* + 0.1$ or $|-\mathrm{E}_0^* - 0.1|$ equals 0.8, however, asymmetry hysteresis loops show up in the PE curves (Figs. 5(B) and 5(C)). If the bias the bias field is applied along the $+x_2$ axis, the asymmetry hysteresis loops will be bigger in the upper half part of the PE curves. When the bias field inverses its direction, the asymmetry hysteresis loops will be bigger in the lower half part. These results indicate again the domain pinning and depinning effect and the role of the critical depinning field. Asymmetry hysteresis loops were observed in real experiment and attributed to the built-in voltages effect.[36] The simulation results provide an alternative explanation for the observed asymmetry hysteresis loop, i.e., the pinning and depinning of domains. As expected, the hysteresis loops will become almost symmetry if the value of $|\mathrm{E}_0^* \pm 0.1|$ is larger than 0.8, as shown in Fig. 5(D).

Figs. 6(a1)–(a4) and 6(b1)–(b4), respectively, show the domain structures corresponding to macroscopic PE points (a1)–(a4) and (b1)–(b4) in Fig. 5(C), illustrating the depinning and pinning phenomena with the positive and negative electric fields. At point (a1) in Fig. 5(C), the positive electric field is larger than the critical depinning electric field, all polarizations above the dislocation array are along the direction of electric field and form a single domain, as shown in Fig. 6(a1), indicating the depinning of domain. However, there is a pinning effect of domain when the electric field is smaller than the critical depinning electric field at point (a4) in Fig. 5(C). Fig. 6(a4)

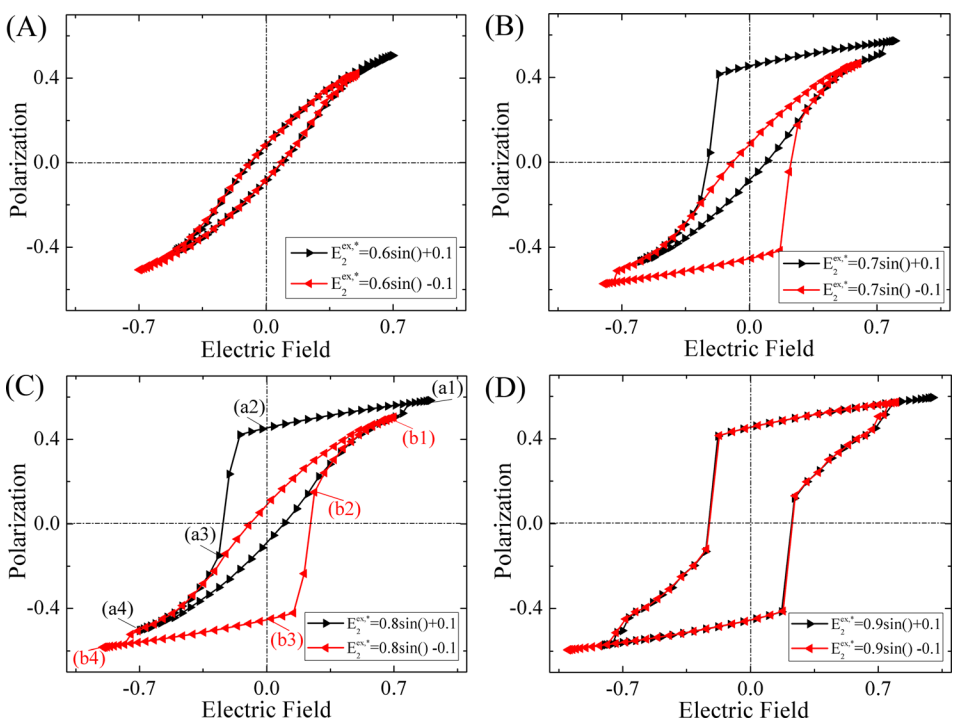

FIG. 5. The effect of a bias field (± 0.1) on the hysteresis loops of the ferroelectric with DLD = 21 and the electric field amplitudes of (A) $\mathrm{E}_0^* = 0.6$, (B) $\mathrm{E}_0^* = 0.7$, (C) $\mathrm{E}_0^* = 0.8$, and (D) $\mathrm{E}_0^* = 0.9$.

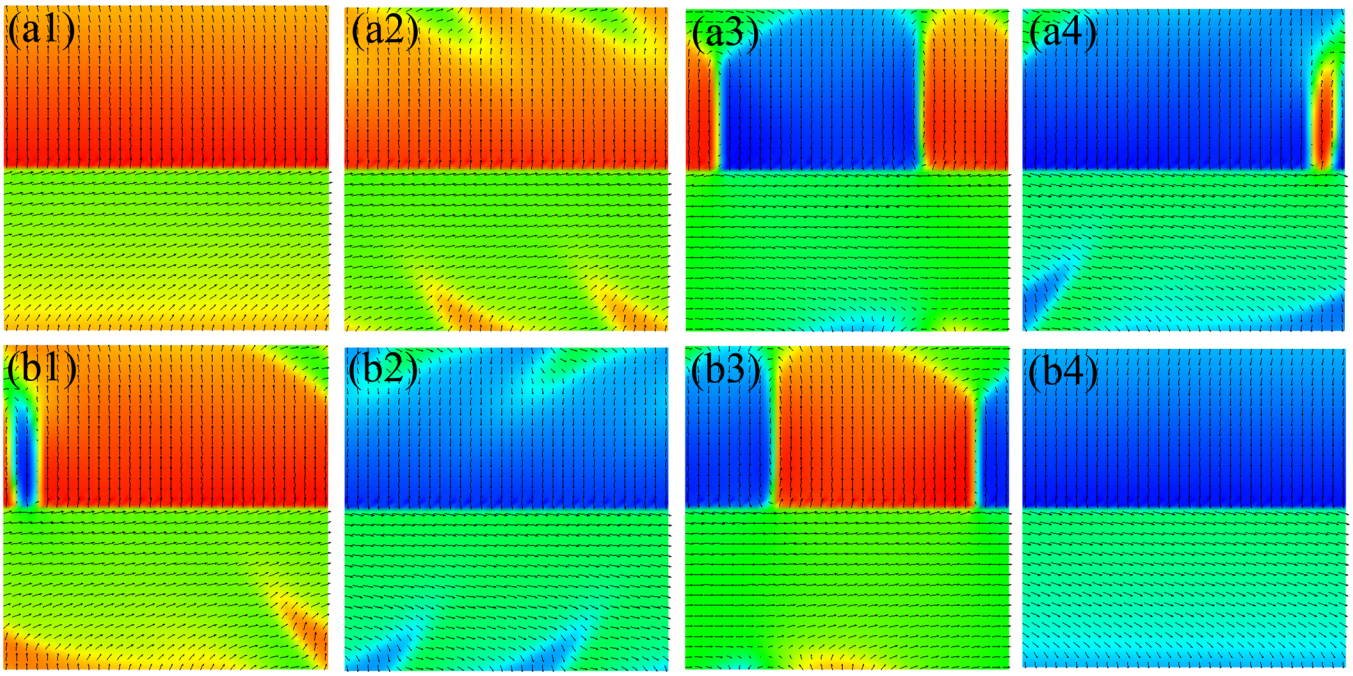

FIG. 6. The domain structures of (a1)–(a4) and (b1)–(b4), respectively, corresponding to points (a1)–(a4) and (b1)–(b4) on the curves of Fig. 5(C) (enhanced online). [URL: http://dx.doi.org/10.1063/1.4826532.3] [URL: http://dx.doi.org/10.1063/1.4826532.4]

shows there are two domains above the dislocation array with polarization antiparallel to electric field, indicating the domain pinning. When the electric field decreases from points (a1) to (a3) in Fig. 5(C), the domain structures above the dislocation array all change from the single domain state to a multi-domain state as shown in Figs. 6(a1)–6(a3), which are similar to those in Figs. 3(b1)–3(b3). The same microstructure evolution results in the same macro-responses of average polarization for the curve (b1), (b2), and (b3) in Fig. 2(C) and the curve (a1), (a2), and (a3) in Fig. 5(C). Similar domain structure evolution occurs under a negative bias field, where the pinning of domain takes place at the positive side of electric field as shown by Fig. 6(b1). When the electric field decreases to zero, the domains with polarizations antiparallel to the field grow and the domains with polarizations parallel to the field shrink, as shown in Fig. 6(b2). When the opposite electric field increases to the coercive field, the polarizations above the dislocation array form a multi-domain state, as shown in Fig. 6(b3). When the opposite electric field exceeds the critical depinning electric field at point (b4) in Fig. 5(C), the multi-domain state converts to a single domain state, as shown in Fig. 6(b4). See Movies 3 and 4 for temporal evolution of the polarization switching process of Fig. 6. For the asymmetry hysteresis loops shown in Figs. 5(B) and 5(C), the coercive field and remanent polarization on one side is much larger than those on other side, which might have potential application in microelectronic and electric industries. Form the discussion, we can see that due to the stress/-strain field of the dislocation array, the pinning and depinning phenomena can be further proved by the intentionally applied bias electric field, while for the case without any dislocation array, even with the external applied bias electric field, both of the remanent polarization and the coercive field will not be affected.

IV. CONCLUSIONS

In summary, the domain pinning and depinning phenomena in a ferroelectric single crystal with dislocation arrays under different external electric fields are investigated by using a phase field model. The domain pinning is different from the conventional domain wall pinning. In domain pinning, domains with polarization direction antiparallel to an applied field can survive under the small applied field amplitude so that no new domain nucleation is needed in the following switching. The present simulations show how domains are pinned by dislocation arrays when the applied electric field amplitude is smaller than a critical level, beyond which domain depinning occurs, antiparallel domain disappear, and new domain nucleation will be needed in the following switching. The critical depinning electric field depends highly on the dislocation spacing in the dislocation arrays. Due to the domain pinning and depinning, asymmetry hysteresis loops could happen when a bias field is applied. The present phase field simulations provide the micro-structural signature and macro-response on the domain pinning and depinning phenomena and mechanism in a ferroelectric single crystal with the dislocation arrays.

ACKNOWLEDGMENTS

This work was financially supported by Hong Kong Research Grants Council (Grant No. 622610), Natural Science Foundation of China (Grant Nos. 11002123 and 11090333), Zhejiang Provincial Natural Science Foundation under Grant No. R6110115, and the United States National Science Foundation under Grant No. DMR-1006541. H. H. Wu acknowledges the support of the oversea awards to visit the Pennsylvania State University from HKUST.

[1]J. F. Scott, Science **315**, 954 (2007).
[2]V. Garcia and M. Bibes, Nature **483**, 279 (2012).
[3]Y. Xiao, V. B. Shenoy, and K. Bhattacharya, Phys. Rev. Lett. **95**, 247603 (2005).
[4]L. Hong, A. K. Soh, Q. G. Du, and J. Y. Li, Phys. Rev. B **77**, 94104 (2008).
[5]I. B. Misirlioglu, A. L. Vasiliev, S. P. Alpay, M. Aindow, and R. Ramesh, J. Mater. Sci. **41**, 697 (2006).
[6]X. Zhu, J. Zhu, S. Zhou, Q. Li, Z. Liu, and N. Ming, Appl. Phys. Lett. **79**, 1345 (2001).
[7]M. W. Chu, I. Szafraniak, R. Scholz, C. Harnagea, D. Hesse, M. Alexe, and U. Gösele, Nature Mater. **3**, 87 (2004).
[8]V. Nagarajan, C. L. Jia, H. Kohlstedt, R. Waser, I. B. Misirlioglu, S. P. Alpay, and R. Ramesh, Appl. Phys. Lett. **86**, 192910 (2005).
[9]P. Gao, C. T. Nelson, J. R. Jokisaari, S. H. Baek, C. W. Bark, Y. Zhang, E. Wang, D. G. Schlom, C. B. Eom, and X. Pan, Nature Commun. **2**, 591 (2011).
[10]W. Shu, J. Wang, and T. Y. Zhang, J. Appl. Phys. **112**, 064108 (2012).
[11]C. A. Randall, N. Kim, J. P. Kucera, W. Cao, and T. R. Shrout, J. Am. Ceram. Soc. **81**, 677 (1998).
[12]J. Shieh, J. E. Huber, and N. A. Fleck, J. Eur. Ceram. Soc. **26**, 95 (2006).
[13]D. N. Fang, Y. H. Zhang, and G. Z. Mao, Theor. Appl. Fract. Mech. **54**, 98 (2010).
[14]C. C. Chou, C. S. Chen, and T.-H. Yeh, Ferroelectrics **380**, 141 (2009).
[15]W. L. Warren, B. A. Tuttle, and D. Dimos, Appl. Phys. Lett. **67**, 1426 (1995).
[16]N. Inoue and Y. Hayashi, IEEE Trans. Electron Devices **48**, 2266 (2001).
[17]X. J. Zheng, Y. C. Zhou, J. M. Liu, and A. D. Li, Surf. Coat. Technol. **176**, 67 (2003).
[18]G. H. Jonker, J. Am. Ceram Soc. **55**, 57 (1972).
[19]Y. L. Li, S. Y. Hu, S. Choudhury, M. I. Baskes, A. Saxena, T. Lookman, Q. X. Jia, D. G. Schlom, and L. Q. Chen, J. Appl. Phys. **104**, 104110 (2008).
[20]S. Y. Hu, Y. L. Li, and L. Q. Chen, J. Appl. Phys. **94**, 2542 (2003).
[21]Y. Zheng, B. Wang, and C. H. Woo, J. Mech. Phys. Solids **55**, 1661 (2007).
[22]A. Kontsos and C. M. Landis, Int. J. Solids Struct. **46**, 1491 (2009).
[23]S. Y. Hu and L. Q. Chen, Acta Mater. **49**, 463 (2001).
[24]T. Mura, "Micromechanics of Defects in Solids" (Kluwer Academic Publisher, Dordrecht, 1982).
[25]H. H. Wu, J. Wang, S. G. Cao, and T. Y. Zhang, Appl. Phys. Lett. **102**, 232904 (2013).
[26]J. Y. Li, C. H. Lei, L. J. Li, Y. C. Shu, and Y. Y. Liu, Acta Mech. Sin. **28**, 915 (2012).
[27]Y. L. Li, S. Y. Hu, Z. K. Liu, and L. Q. Chen, Acta Mater. **50**, 395 (2002).
[28]J. Wang, S. Q. Shi, L. Q. Chen, Y. Li, and T. Y. Zhang, Acta Mater. **52**, 749 (2004).
[29]A. K. Tagantsev, Ferroelectrics **375**, 19 (2008).
[30]C. H. Woo and Y. Zheng, Appl. Phys. A **91**, 59 (2008).
[31]P. Wu, X. Ma, Y. Li, V. Gopalan, and L. Q. Chen, Appl. Phys. Lett. **100**, 092905 (2012).
[32]J. Wang and T. Y. Zhang, Phys. Rev. B **73**, 144107 (2006).
[33]Y. Li, S. Li, and T. Y. Zhang, J. Nucl. Mater. **395**, 120 (2009).
[34]L. Q. Chen and J. Shen, Comput. Phys. Commun. **108**, 147 (1998).
[35]W. Cao, Nature Mater. **4**, 727 (2005).
[36]W. F. Liu, S. Y. Wang, and C. Wang, Physica B **406**, 3406 (2011).